

First principles based multiparadigm modeling of electronic structures and dynamics

Thesis by

Hai Xiao

In Partial Fulfillment of the Requirements

for the Degree of

Doctor of Philosophy



California Institute of Technology

Pasadena, California

2015

(Defended January 15, 2015)

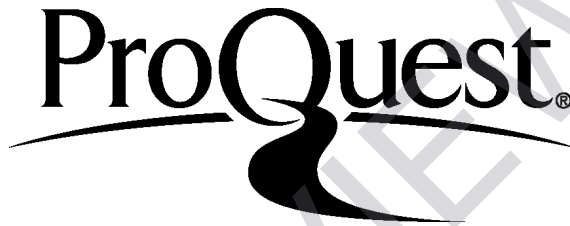
ProQuest Number: 3731108

All rights reserved

INFORMATION TO ALL USERS

The quality of this reproduction is dependent upon the quality of the copy submitted.

In the unlikely event that the author did not send a complete manuscript and there are missing pages, these will be noted. Also, if material had to be removed, a note will indicate the deletion.



ProQuest 3731108

Published by ProQuest LLC (2015). Copyright of the Dissertation is held by the Author.

All rights reserved.

This work is protected against unauthorized copying under Title 17, United States Code
Microform Edition © ProQuest LLC.

ProQuest LLC.
789 East Eisenhower Parkway
P.O. Box 1346
Ann Arbor, MI 48106 - 1346

PREVIEW

© 2015

Hai Xiao

All Rights Reserved

To the memory of my grandma Ding-Xiang and grandpa Yong-Chu
and
to my wife Ying and our son Jun

PREVIEW

Acknowledgments

I wish to thank my advisor, Prof. Bill Goddard, for his constant support and guidance over the past six years. I appreciate very much the flexibility Bill offered me in both choosing research topics and working pace, as well as the broad knowledge of theory, modeling, and experiments he shared with me, and the key ideas he proposed that greatly sped up my research progress.

I would like to thank other group members I have collaborated with: Julius T. Su, Jamil Tahir-Kheli, Andrés Jaramillo-Botero, Patrick L. Theofanis, Sergey V. Zybin, Wei-Guang Liu, Qi An, and Sijia Dong. Additionally, I have also enjoyed in our group chatting and friendship with Mu-Jeng Cheng, Sha Yao, Wei-Guang Liu, Qi An, Yi Liu, Ted Yu, Himanshu Mishra, Fan Liu, Lianchi Liu, Tingting Zhou, Vaclav Cvicek, Ho-Cheng Tsai, Tao Cheng, Sijia Dong, and José Mendoza-Cortes. It's quite a pleasure being a member of this big family.

I would like to thank my committee members, Prof. Harry Gray, Prof. Rudy Marcus, and Prof. Nate Lewis, for constructive comments and discussions on my candidacy, proposals, and thesis. I would also like to thank my candidacy committee chair, Prof. Aron Kuppermann, who is not with us any more, for his caring about both my research and life in the early stage of my graduate student life.

I would love to thank all my friends, though it's too big a list to put here, for helping me get through rough times and enriching my life these years.

Finally I would like to thank my parents for unconditional love and support, and I wish to thank my wife Ying. Ying and I have been together for more than ten years, and I dread to think what my life would be without her. I would very much love to dedicate this thesis to her and our beloved son Jun.

List of Abbreviations

QM	quantum mechanics
BO	Born-Oppenheimer
PES	potential energy surface
MD	molecular dynamics
HF	Hartree-Fock
UHF	unrestricted Hartree-Fock
VB	valence bond
GVB	generalized valence bond
TDHF	time-dependent Hartree-Fock
DFT	density functional theory
TDDFT	time-dependent density functional theory
KS	Kohn-Sham
GKS	generalized Kohn-Sham
XC	exchange and correlation
LDA	local density approximation
GGA	generalized gradient approximation
meta-GGA	meta-generalized gradient approximation
AO	atomic orbital
MO	molecular orbital
HOMO	highest occupied molecular orbital
LUMO	lowest unoccupied molecular orbital
VBM	valence band maximum
CBM	conduction band minimum
VBO	valence band offset
CBO	conduction band offset
DOS	density of states
SOC	spin-orbit coupling
ECP	effective core potential

USPP	ultrasoft p seudopotential
PAW	projector a ugmented- w ave
BSSE	basis set superposition e rror
PBC	periodic b oundary c onditions
IP	ionization p otential
EA	electron a ffinity
AEP	average e lectrostatic p otential
EOS	equation o f state
ZPE	zero p oint e nergy
TS	transition state
eFF	electron force field
FSG	floating spherical G aussian
EOM	equations o f m otion
GHA-QM	G aussian H artree approximated q uantum mechanics
AMPERE	angular m omentum p rojected e ffective core pseudopotential
MAD	mean a bsolute d eviation
MRD	mean r elative d eviation
RMSD	root m ean s quare d eviation
GA	genetic algorithm
<i>n</i>D	<i>n</i> = 0, 1, 2, 3 dimensional
CIGS	CuIn_xGa_{1-x}Se₂

Abstract

Electronic structures and dynamics are the key to linking the material composition and structure to functionality and performance.

An essential issue in developing semiconductor devices for photovoltaics is to design materials with optimal band gaps and relative positioning of band levels. Approximate DFT methods have been justified to predict band gaps from KS/GKS eigenvalues, but the accuracy is decisively dependent on the choice of XC functionals. We show here for CuInSe_2 and CuGaSe_2 , the parent compounds of the promising CIGS solar cells, conventional LDA and GGA obtain gaps of 0.0–0.01 and 0.02–0.24 eV (versus experimental values of 1.04 and 1.67 eV), while the historically first global hybrid functional, B3PW91, is surprisingly the best, with band gaps of 1.07 and 1.58 eV. Furthermore, we show that for 27 related binary and ternary semiconductors, B3PW91 predicts gaps with a MAD of only 0.09 eV, which is substantially better than all modern hybrid functionals, including B3LYP (MAD of 0.19 eV) and screened hybrid functional HSE06 (MAD of 0.18 eV).

The laboratory performance of CIGS solar cells ($> 20\%$ efficiency) makes them promising candidate photovoltaic devices. However, there remains little understanding of how defects at the CIGS/CdS interface affect the band offsets and interfacial energies, and hence the performance of manufactured devices. To determine these relationships, we use the B3PW91 hybrid functional of DFT with the AEP method that we validate to provide very accurate descriptions of both band gaps and band offsets. This confirms the weak dependence of band offsets on surface orientation observed experimentally. We predict that the CBO of perfect $\text{CuInSe}_2/\text{CdS}$ interface is large, 0.79 eV, which would dramatically degrade performance. Moreover we show that band gap widening induced by Ga adjusts only the VBO, and we find that Cd impurities do not significantly affect the CBO. Thus we show that Cu vacancies at the interface play the key role in enabling the tunability of CBO. We predict that Na further improves the CBO through electrostatically elevating the valence levels to decrease the CBO, explaining the observed essential role of Na for high performance. Moreover we find that K leads to a dramatic decrease in the CBO to 0.05 eV, much better than Na. We suggest that the efficiency of CIGS devices might be improved substantially by tuning the ratio of Na to K, with the improved phase stability of Na balancing phase instability from K. All these defects reduce interfacial stability slightly, but not significantly.

A number of exotic structures have been formed through high pressure chemistry, but applications have been hindered by difficulties in recovering the high pressure phase to ambient conditions (i.e., one atmosphere and room temperature). Here we use dispersion-corrected DFT (PBE-*ulg* flavor) to predict that above 60 GPa the most stable form of N_2O (the laughing gas in its molecular form) is a 1D polymer with an all-nitrogen backbone analogous to *cis*-polyacetylene in which alternate N are bonded (ionic covalent) to O. The analogous *trans*-polymer is only 0.03–0.10 eV/molecular unit less stable. Upon relaxation to ambient conditions both polymers relax below 14 GPa to the same stable non-planar *trans*-polymer, accompanied by possible electronic structure transitions. The predicted phonon spectrum and dissociation kinetics validate the stability of this *trans*-poly-NNO at ambient conditions, which has potential applications as a new type of conducting polymer with all-nitrogen chains and as a high-energy oxidizer for rocket propulsion. This work illustrates *in silico* materials discovery particularly in the realm of extreme conditions.

Modeling non-adiabatic electron dynamics has been a long-standing challenge for computational chemistry and materials science, and the eFF method presents a cost-efficient alternative. However, due to the deficiency of FSG representation, eFF is limited to low- Z elements with electrons of predominant s -character. To overcome this, we introduce a formal set of ECP extensions that enable accurate description of p -block elements. The extensions consist of a model representing the core electrons with the nucleus as a single pseudo particle represented by FSG, interacting with valence electrons through ECPs. We demonstrate and validate the ECP extensions for complex bonding structures, geometries, and energetics of systems with p -block character (C, O, Al, Si) and apply them to study materials under extreme mechanical loading conditions.

Despite its success, the eFF framework has some limitations, originated from both the design of Pauli potentials and the FSG representation. To overcome these, we develop a new framework of two-level hierarchy that is a more rigorous and accurate successor to the eFF method. The fundamental level, GHA-QM, is based on a new set of Pauli potentials that renders exact QM level of accuracy for any FSG represented electron systems. To achieve this, we start with using exactly derived energy expressions for the same spin electron pair, and fitting a simple functional form, inspired by DFT, against open singlet electron pair curves (H_2 systems). Symmetric and asymmetric scaling factors are then introduced at this level to recover the QM total energies of multiple electron pair systems from the sum of local interactions. To complement the imperfect FSG representation, the AMPERE extension is implemented, and aims at embedding the interactions associated with both the cusp condition and explicit nodal structures. The whole GHA-QM+AMPERE framework is tested on H element, and the preliminary results are promising.

Contents

Acknowledgments	iv
List of Abbreviations	v
Abstract	vii
List of Figures	xi
List of Tables	xiii
1 Introduction	1
References	2
2 Accurate description of electronic structures for semiconductors from DFT	3
2.1 Fundamental band gap from KS/GKS scheme in DFT	4
2.2 Choice of basis sets and ECPs for periodic calculations	6
2.3 Key ingredients in XC functionals for performance	8
2.4 Benchmark on a set of 27 binary and ternary semiconductors	11
2.5 Concluding remarks	15
Appendix	15
References	21
3 Predicted roles of defects in band offsets and energetics at CIGS Solar Cell interfaces and implications for improving performance	27
3.1 Methodology for calculating band offsets from interface modeling	28
3.2 Band offsets at pristine CIGS/CdS interfaces	31
3.3 Bulk structures of defect CIGS	33
3.4 Roles of defects in band offsets and energetics at CIGS/CdS interfaces	36
3.5 Concluding remarks	38
Appendix	39
References	43

4	Formation of the --N(NO)N(NO)-- polymer at high pressure and stabilization at ambient conditions	49
4.1	Search for extended solid phases of N_2O under high pressures	50
4.2	Transitions between molecular, ionic, and polymer phases of N_2O	51
4.3	Relaxation of polymer phases to ambient conditions	54
4.4	Kinetic stability of the non-planar N_2O polymer at ambient conditions	59
4.5	Concluding remarks	60
	Appendix	61
	References	63
5	Development of ECP for eFF to extend application to high-Z elements	67
5.1	Formulation of ECP models in eFF	69
5.2	Performance of optimized eFF-ECP parameters	72
5.2.1	Al and Si with s - s ECP	73
5.2.2	C with s - p ECP	75
5.2.3	Oxygen with s - p ECP	78
5.2.4	Silicon carbide with combined s - s and s - p eFF-ECP	80
5.3	Conclusions	81
	References	82
6	Gaussian Hartree approximated QM with angular momentum projected effective core pseudopotential	85
6.1	Exact QM energies of same spin FSG electron pair	86
6.2	Symmetric and asymmetric scaling factors for same spin Pauli potential	90
6.3	Design of opposite spin Pauli potential	93
6.4	The AMPERE extension	97
6.5	Concluding remarks and future work	101
	Appendix	101
	A. Series expansions of ΔT , ΔC_{ee} , and ΔC_{ne}	101
	B. A hybrid scheme to construct opposite spin Pauli potential	102
	C. Integrals involved in energy evaluation with AMPERE	105
	D. Numerical implementation of AMPERE (<code>pair_eff_ecp.h</code>) in LAMMPS	108
	References	114

List of Figures

2.1	The band structure and DOS of CuInSe ₂ calculated with B3PW91.	9
2.2	The band structure and DOS of CuGaSe ₂ calculated with B3PW91.	10
3.1	Illustration of the computation of band offsets for the CuInSe ₂ /CdS (110) interface.	30
3.2	The CuInSe ₂ /CdS (112) polar interface model and the calculated band alignment.	32
3.3	The interface models and calculated band alignments of CuIn _{0.75} Ga _{0.25} Se ₂ /CdS.	33
3.4	DOS of Cu-rich CuInSe ₂ shows the dominance of Cu 3 <i>d</i> in the valence region.	34
3.5	The lowest energy model crystal structures for Cu ₅ In ₉ Se ₁₆ and CuIn ₅ Se ₈	35
3.6	The interface models and calculated band alignments of Cu ₅ In ₉ Se ₁₆ /CdS and CuIn ₅ Se ₈ /CdS.	36
3.7	DOS of Cu-poor CuIn ₅ Se ₈ shows the dominance of Se 4 <i>p</i> in the valence region.	37
3.8	The interface models and calculated band alignments of Na ₂ Cu ₃ In ₉ Se ₁₆ /CdS, K ₂ Cu ₃ In ₉ Se ₁₆ /CdS and CdCu ₃ In ₉ Se ₁₆ /CdS.	38
4.1	Illustration of crystal structures and chemical formulations of a single chain for planar <i>cis</i> -polymer and planar <i>trans</i> -polymer.	51
4.2	Ground state enthalpy as a function of pressure predicted for various phases of N ₂ O.	52
4.3	Comparison between PBE- <i>ulg</i> calculated and experimental EOSs for molecular phases of N ₂ O.	53
4.4	Illustration of the orthorhombic crystal structure of ionic NO ⁺ NO ₃ ⁻ with space group <i>Pna2</i> ₁	54
4.5	The effect of quantum ZPE and temperature (entropy) on the transition pressure to polymer phase <i>P_c</i>	55
4.6	Phonon spectra for polymer phases of N ₂ O predicted at 80 and 0 GPa.	56
4.7	Illustration of crystal structure and chemical formulation of a single chain for non- planar <i>trans</i> -polymer.	57
4.8	Band gap and neighboring N–N bond length difference predicted as functions of pres- sure for all three polymer phases of N ₂ O at ground states.	58

4.9	Total and partial electronic DOSs calculated with B3PW91 for planar <i>cis</i> - and <i>trans</i> -polymers at 80 GPa.	58
4.10	Reaction path calculated for dissociation of the model oligomer.	59
4.A1	EOSs for various phases of N ₂ O at ground states.	61
4.A2	TS calculated for dissociation of an isolated periodic infinite chain of the non-planar polymer.	61
5.1	eFF aims at long term and large scale non-adiabatic MD simulations.	68
5.2	Illustration of distances used in the two functional types of ECP.	70
5.3	Comparison of cluster bond energies for different Al _n H _{3n} clusters.	74
5.4	Crack tip velocity versus reduced load for {111} fracture from eFF-ECP, compared to experimental, ReaxFF+Tersoff simulations, and DCET and EDIP data.	75
5.5	Mechanism of local field-induced ionization.	76
5.6	Gallery of molecules with conjugate double bonds.	77
5.7	Comparison of various methods on the binding curve along the dispersion <i>c</i> axis of graphite.	78
5.8	Illustration of electronic excitation-induced desorption of hydrogen from a passivated diamond slab.	79
5.9	Open shell like representation of lone pairs in eFF-ECP.	79
6.1	Comparison of different energy contributions upon antisymmetrization for total energies of triplet H ₂ system.	88
6.2	Comparison of different energy contributions upon antisymmetrization for optimizing electron wavefunctions of triplet H ₂ system.	89
6.3	Benchmark of eFF, GHA-QM with and without scaling.	90
6.4	Performance of symmetric scaling factor functions.	92
6.5	Performance of asymmetric scaling factor functions.	92
6.6	Fitting of opposite spin Pauli potential against open singlet H ₂ at B3LYP level. . . .	94
6.7	Performance of GHA-QM on the open singlet and triplet H ₂ systems.	95
6.8	Performance of GHA-QM on symmetric stretching in <i>D</i> _{∞h} H ₃ and <i>D</i> _{4h} H ₄	96
6.9	Performance of GHA-QM on asymmetric stretching in <i>D</i> _{∞h} H ₃ and <i>D</i> _{4h} H ₄	96
6.10	Decomposition of valence FSG wavefunction into core-centered orbitals with various angular momenta.	98
6.11	Performance of GHA-QM+AMPERE on the dissociation curve of H ₂ molecule. . . .	100
6.B1	Performance of fitting of prefactors on open singlet H ₂ at UHF level.	103
6.B2	Performance of the hybrid scheme on open singlet H ₂ at UHF and B3LYP levels. . .	104

List of Tables

2.1	Comparison of the performance of pruned and optimized basis sets on structures and band gaps of CuInSe ₂ , CuGaSe ₂ , and CdS.	7
2.2	Predicted band gap and lattice parameters for CuInSe ₂ chalcopyrite crystal from various levels of XC functionals.	9
2.3	Predicted band gap and lattice parameters for CuGaSe ₂ chalcopyrite crystal from various levels of XC functionals.	10
2.4	Predicted band gaps (eV) for 27 semiconductors with B3PW91 (MAD = 0.09 eV). .	12
2.5	Predicted lattice parameters ($a/\text{\AA}$) for 9 binary semiconductors with B3PW91 (MRD = 1.9%).	12
2.6	Predicted lattice parameters for 18 ternary semiconductors with B3PW91 (MRD = 2.2%).	12
2.7	Predicted band gaps (eV) for 27 semiconductors with B3LYP (MAD = 0.19 eV). .	13
2.8	Predicted lattice parameters ($a/\text{\AA}$) for 9 binary semiconductors with B3LYP (MRD = 3.1%).	13
2.9	Predicted lattice parameters for 18 ternary semiconductors with B3LYP (MRD = 3.6%).	13
2.10	Predicted band gaps (eV) for 27 semiconductors with HSE06 (MAD = 0.18 eV). .	14
2.11	Predicted lattice parameters ($a/\text{\AA}$) for 9 binary semiconductors with HSE06 (MRD = 1.6%).	14
2.12	Predicted lattice parameters for 18 ternary semiconductors with HSE06 (MRD = 2.0%).	14
3.1	Convergence of interface thickness (d), interfacial energy (σ), VBO (ΔE_v), and CBO (ΔE_c) with respect to number of layers of each side (L) and the interface-interface distance (D) for CuInSe ₂ /CdS interfaces parallel to (110) and (112).	31
3.2	Fluctuations in calculated CBO values from using core levels of different elements. .	32
3.3	Relative energies (ΔE) in meV/atom of all possible configurations within a $\sqrt{2} \times \sqrt{2} \times 1$ supercell for Cu ₅ In ₉ Se ₁₆ phase calculated with B3PW91.	35
3.4	Relative energies (ΔE) in meV/atom of low energy configurations for CuIn ₅ Se ₈ phase calculated with B3PW91 and PBE.	35

5.1	eFF-ECP parameters optimized for a few 2 nd and 3 rd row <i>p</i> -block elements.	72
5.2	Comparison of eFF-ECP, all electron eFF and DFT calculations on aluminum hydrides.	73
5.3	Comparison of eFF-ECP and eFF on geometries of carbon-containing molecular and bulk systems.	76
5.4	Performance of eFF-ECP on geometries of various molecules with oxygen atom(s).	80
5.5	Carbon <i>s-p</i> functional form parameters in the SiC-ECP force field and Silicon <i>s-s</i> parameters from Ref. [8].	80
5.6	Silicon Carbide training set and optimization results using the <i>s-p</i> form ECP for Carbon.	81
6.1	Fitted parameters for asymmetric scaling factor functions.	91
6.2	Fitted parameters for $E_{\text{Pauli}}^{\text{base}}(\uparrow\downarrow)$	94
6.B1	Fitted parameters for the prefactors at UHF level.	104

Chapter 1

Introduction

There is no doubt that MO and VB theory play a pivotal role in shaping chemists' understanding of chemistry, and elegant models and concepts have been derived, such as resonance, hybridization, VSEPR theory, Walsh diagram, ligand field theory, and frontier MO theory, to name but a few. Electronic structure, as a more generalized term, naturally covers the concepts ranging from orbital and bonding of finite molecules to bands and DOS of extended phases, and thus provides a bridging concept between chemistry and material science. Such crossing has lead to insightful perspective and delicate understanding (see, e.g., [1] and [2]). Modern computational modeling techniques have enabled accurate quantitative description of electronic structures, which is the key to unveiling the relationship between chemical composition and material functionality. The first half of this thesis (Ch. 2–Ch. 4) is devoted to such research, in which predictions were made for the dependence of device performance on underlying material composition and the formation of novel functional material, through understanding the electronic structures by using DFT methods. As a preliminary, Ch. 2 discusses the physical significance of HOMO (VBM) and LUMO (CBM) from approximate DFT, and then elaborates on our choices of methodology based on benchmark calculations. Subsequently, Ch. 3 presents our appreciation of CIGS solar cell performance via modeling of band offsets across the CIGS/CdS interfaces, and Ch. 4 proposes a novel N₂O polymer, with alternating single and double bonds along the all-nitrogen backbone, which is formed under high pressures and stabilized by conformational relaxation at ambient conditions, and its electronic structure transition associated with structural change is discussed in details.

Accurate first principles methods such as DFT are currently capable of handling up to thousands of atoms, but for practical consideration, very large scale and long term simulations, inevitable under many scenarios such as amorphous and liquid phases, biomolecules, and phase transitions etc., are mostly employing empirical force field methods. Among these methods, ReaxFF[3] in particular is termed as first principles based, in the sense that its underlying functional forms are inspired by QM ideas and its parameters are fitted against database constructed with first principles methods. However, electronic structures are just implicitly and partly accounted for by parameterization

in terms like bond order and coordination, and the absence of explicit electron densities leads to problems (though solvable with extra effort) in phenomena like lone pairs, polarization, and charge variation. Besides, under certain circumstances such as high velocity shock and extreme conditions (high temperatures in particular), the electronic dynamics (propagation) is significantly involved and should be taken into account. The eFF method[4], originally developed in our group, provides the suitable first principles based framework to address the above issues, and the second half of this thesis (Ch. 5–Ch. 6) is then devoted to our effort to improve it. Ch. 5 describes our very early work in extending the application of eFF method to high- Z elements by developing an ECP extension for it, while more importantly, Ch. 6 presents our very recent development of the new GHA-QM+AMPERE framework that is a more rigorous and accurate successor of the eFF method.

The above-mentioned two parts on modeling of electronic structures and dynamics complete this thesis, and the variation in levels of theory involved, from hybrid XC functionals and dispersion correction of DFT to eFF and GHA-QM+AMPERE methods, endows it with a multiparadigm character. Therefore, this thesis is ultimately titled as “First principles based multiparadigm modeling of electronic structures and dynamics”.

References

- [1] Hoffmann, R. (1988) *Solids and Surfaces: A Chemist's View on Bonding in Extended Structures*. (VCH Publishers, Inc., New York).
- [2] Burdett, J. K. (1995) *Chemical Bonding in Solids*. (Oxford University Press, Inc., New York).
- [3] van Duin, A. C. T, Dasgupta, S, Lorant, F, & Goddard, W. A. (2001) ReaxFF: A reactive force field for hydrocarbons. *J. Phys. Chem. A* **105**, 9396–9409.
- [4] Su, J. T. (2007) Ph.D. thesis (California Institute of Technology).

Chapter 2

Accurate description of electronic structures for semiconductors from DFT

The contents presented in this chapter are based on [H. Xiao, J. Tahir-Kheli and W. A. Goddard, III, “Accurate Band Gaps for Semiconductors from Density Functional Theory”, *J. Phys. Chem. Lett.* **2011**, *2*, 212-217.](#)

An essential issue in developing semiconductor devices for photovoltaics is to design materials with desirable characters of electronic structures, ranging from such simple properties as appropriate band gaps and proper positioning of band levels relative to other participating members (dopants and interfacing materials, etc.), to convoluted aspects like good-natured band curvatures and wave-functions for efficient transport of photo-excited species (excitons and charge carriers). Accurate theoretical modeling of electronic structures for semiconductors stands as a powerful tool for unveiling the correlation of relevant features and functionalities to the underlying material compositions and structures, and thus plays an indispensable role in both improving the performance of current devices and conceiving novel photovoltaic materials.

DFT[1–3] proves an extremely valuable theoretical framework as elegant compromise between computational efficiency and accuracy, and various levels of approximate XC functionals have demonstrated extensively predictive power for energetics, structures, and dynamics of systems, ranging from 0D finite molecules to 3D periodic solids. However, the XC functionals at LDA and GGA levels, traditionally and exclusively used in the solid state physics community, suffer from serious underestimation of band gaps for semiconductors and insulators, and even qualitatively wrong prediction of metallic states for some small band gap ($< \sim 1$ eV) systems, while the hybrid functionals, being the superior standard choice in the quantum chemistry community from early on, have recently gained popularity in modeling of periodic systems, largely owing to growing evidence that shows their ability to predict band gaps accurately for semiconductors.

This chapter describes our work[4] on benchmarking the performance of DFT methods on band gaps of semiconductors relevant to photovoltaic applications. The theoretical background for using the KS/GKS orbital energy gap as a prediction of fundamental band gap is outlined in Sec. 2.1. Sec. 2.2 discusses the choice of basis sets and ECP and describes the computational details for our periodic calculations. Sec. 2.3 determines the best XC functionals by comparing performance of various levels of XC functionals on CuInSe₂ and CuGaSe₂, and Sec. 2.4 benchmarks B3PW91, B3LYP, and HSE06 over a set of 27 binary and ternary semiconductors.

2.1 Fundamental band gap from KS/GKS scheme in DFT

Although orbitals and associated eigenvalues (orbital energies) in the KS/GKS scheme have been widely discussed for their interpretative power within qualitative MO theories and approximation to such physical observables as IP[5–10], strictly speaking, KS/GKS orbitals are by construct solutions to the one-electron equations for artificial non-interacting system used to approximate the exact ground state, and thus have no rigorous physical significance in general[11]. However, similar to Koopmans’ theorem[12] in HF theory, which relates the eigenvalue of HOMO $\epsilon_{\text{HOMO}}^{\text{HF}}$ as an approximation to the first IP I , i.e., $\epsilon_{\text{HOMO}}^{\text{HF}} \approx -I$, it has been proven[13, 14] that in DFT, the HOMO eigenvalue from *exact* KS theory (*exact* XC functional) is precisely the negative of IP, i.e., $\epsilon_{\text{HOMO}}^{\text{KS}} = -I$, provided that the KS effective local potential vanishes at infinity. Furthermore, it was shown recently[15, 16] that the LUMO with its eigenvalue in KS/GKS scheme carries as much information on electron addition (associated energy as EA) as the HOMO does on electron removal.

Such relations set up the theoretical background of DFT’s ability to predict an important figure, the difference between IP and EA, which defines the chemical hardness η with a prefactor of 1/2 for finite species[17], or the fundamental band gap E_g for periodic systems, as

$$E_g = I - A = [E(N-1) - E(N)] - [E(N) - E(N+1)] = \left. \frac{\partial E}{\partial N} \right|_{N+\delta} - \left. \frac{\partial E}{\partial N} \right|_{N-\delta} \quad (2.1)$$

where E and N are the total energy and number of electrons, respectively. The last step in (2.1) is valid, provided that E is a series of straight lines interpolating values at integer N ’s, and such character is shown to be possessed by the exact energy functional[13, 18], and also ostensibly by the approximate XC functionals (including the nonlocal HF exchange functional in GKS scheme) for periodic systems imposed by the translational symmetry[19]. According to the conventional density functional analysis[20, 21], (2.1) can be further evaluated as

$$E_g = \epsilon_{\text{LUMO}}^{\text{KS}} - \epsilon_{\text{HOMO}}^{\text{KS}} + \Delta_{\text{XC}} \quad (2.2)$$

where $\Delta_{\text{XC}} = v_{\text{XC}}^{(+)} - v_{\text{XC}}^{(-)} \equiv \left. \frac{\delta E_{\text{XC}}[\rho]}{\delta \rho} \right|_{N+\delta} - \left. \frac{\delta E_{\text{XC}}[\rho]}{\delta \rho} \right|_{N-\delta}$ is the functional derivative discontinuity of XC energy with respect to the density (this term is non-vanishing for the *exact* case), which apparently prevents direct prediction of E_g using the KS orbital energy gap in DFT. While a more recent perspective, analyzing E as a functional of one-electron potential v_s and N (the so-called potential functional formalism)[22, 23], elaborates (2.1) in various types of approximate XC functionals[15, 16], and for the two cases we are interested in,

Case A KS scheme where E_{XC} is an explicit and differentiable functional of ρ only (e.g., LDA and GGA)

Case C GKS scheme where E_{XC} is an explicit and differentiable functional of the first order non-interacting density matrix, and the noninteracting reference system has a nonlocal GKS potential (e.g., HF calculations)

both simplify (2.1) into, with the orbitals $\{\phi_i\}$ as the only minimizer,

$$E_g = \varepsilon_{\text{LUMO}}^{\text{KS/GKS}} - \varepsilon_{\text{HOMO}}^{\text{KS/GKS}} \quad (2.3)$$

which is still consistent with (2.2) from the conventional density functional analysis, because for Case A, the approximate XC functionals render a vanishing Δ_{XC} (in contrast to the unknown *exact* XC functional), and for Case C, the discontinuity of $\frac{\partial \rho}{\partial N}$ distributes contribution of Δ_{XC} to eigenvalues of the minimizer $\{\phi_i\}$. (2.3) justifies rigorously the use of KS/GKS orbital energy gap as a direct prediction of the fundamental band gap for commonly used XC functionals (LDA, GGA, and hybrid functionals), with the accuracy dictated by the levels of approximations employed, although it must be borne in mind that (2.3) does not hold for the *exact* XC functional, if ever known.

Now the question is what level of approximation should be chosen for practical use in prediction of fundamental band gaps with sufficient accuracy for certain materials, and recent analysis of total energy for fractional charges[15, 19, 24] offers some theoretical insights: conventional DFT XC functionals such as LDA and GGA result in convex curves (lower energies) for fractional charges in-between integer numbers of electrons, in contrast to the straight lines given by the *exact* case, while the HF theory renders concave curves (higher energies); such incorrect features originate from the tendency of underlying approximations to delocalize/localize electrons, which is thus termed as delocalization/localization error; the convex/concave curves are forced into straight lines in periodic systems by the imposed translational symmetry, which follow the initial slopes of the original curves, leading to underestimated/overestimated fundamental band gaps. This analysis constitutes the theoretical foundation for the superiority of hybrid functionals, which include both GGA and HF components, and thus the delocalization and localization errors cancel out, to a certain extent, but the mixed percentage of HF exchange is in principle dependent on the system under study.

Indeed, it has been demonstrated by benchmark calculations on quite a range of materials[4, 25–29] that including some exact HF exchange in the global and screened hybrid functional schemes leads to dramatically improved prediction of band gaps, and among these efforts our work[4] was originally motivated by the study of properties of the CIGS class of solar cells, pioneered by the National Renewable Energy Laboratory (NREL), with efficiencies as high as 20.3%[30]. The heterojunction in these devices is between *n*-type CdSe and a *p*-type alloy of CuGaSe₂ and CuInSe₂ (with atomic ratios, Cu/(In+Ga) = 0.80-0.92 and Ga/(In+Ga) = 0.30-0.35). The important issues here are the magnitude of the direct band gap and the offsets in the band states at the interfaces as a function of composition. We were disappointed to find that the PBE and PW91 of GGA level lead to a band gap for CuInSe₂ of $E_g = 0.01$ eV (LDA leads to zero band gap) compared to the experimental value of $E_g = 1.04$ eV. Moreover, the popular B3LYP hybrid functional (which obtains the correct band gap of 2.0 eV for La₂CuO₄[27]) leads to $E_g = 0.95$ eV, which is too small by 9%. This led us to explore the performance of other DFT methods, and further show that the historically first hybrid density functional, B3PW91, leads to substantially better prediction of band gaps for the binary and ternary semiconductor compounds that are of interest in photovoltaics.

2.2 Choice of basis sets and ECPs for periodic calculations

Conceptually, plane wave basis sets are the best choice for periodic calculations, in a few respects: orthogonality (free of linear dependency), completeness (straightforward to improve the quality), no dependence of nuclear positions (no associated Pulay forces[31]), and infinite periodicity (PBC in nature and no BSSE), among others. In practice, however, plane wave basis sets demand extra efforts: one is the necessity of pseudopotentials for the atomic core region (even for light elements like H), due to the formidable number of plane waves required to sufficiently approximate the sharp electron density in the vicinity of nuclei; another is the complexity for evaluating HF exchange due to its nonlocal nature, and the computation is 10^2 - 10^3 times slower than with the localized atom-centered Gaussian type basis sets, making the modeling of even medium-sized systems ($\sim 10^2$ atoms) extremely expensive. Therefore, for hunting the best among XC functionals, including hybrid ones, for practical use (see Ref. [32] and Ch. 3), all calculations were performed using the CRYSTAL package[33], which employs atomic Gaussian type basis sets for periodic systems.

For heavy elements, angular-momentum-projected nonlocal ECPs[34–37] were used to replace the core electrons, for both reducing the computational cost and, more importantly, incorporating implicitly scalar relativistic effects. SOC was not explicitly treated, which can be important in determining band gaps for certain heavy systems[38, 39], and thus here band gaps are averaged over the spin-orbit levels through ECPs. The specific choice of ECPs and basis sets are summarized below:

- for Cu, Ag, Zn, Cd, Ga, and In we used the shape-consistent[40, 41] fully relativistic SBKJC small core ECPs with double zeta basis sets[42]
- for As and Sb we used the energy-consistent[43] fully relativistic Stuttgart small core ECPs[44] with cc-pVDZ basis sets[45]
- for Se and Te we used the SBKJC large core ECPs with double zeta basis sets[42] augmented by one d polarization function[46]
- for Al, P, and S we used the all-electron 6-31G(*d*) basis sets[47]

The difference between small and large core ECPs is whether electrons in the second outmost main shell are explicitly treated, e.g., for Ga, 21 electrons ($3s^23p^63d^{10}4s^24p^1$) are explicitly included in the calculations, with the small core ECP representing the Ne($1s^22s^22p^6$) core, while Se is described with only 6 electrons ($4s^24p^4$), with the large core ECP representing the $1s^22s^22p^63s^23p^63d^{10}$ core. All basis sets were modified slightly by setting any exponents more diffuse than 0.10 to this value (see Appendix for detailed modification in basis sets). This pruning procedure is necessary in order to minimize linear dependency and improve numerical instability for crystalline calculations using molecular basis sets[29]. Ideally, exponents and coefficients in these molecular basis sets should be re-optimized in crystalline calculations. Table 2.1 lists the comparison of performance with pruned basis sets as described above, to with basis sets optimized for crystalline calculations (see Ch. 3 Appendix and Ref. [32]), and both structures, including lattice parameters and internal degree of freedom $u(\text{Se})$, and band gaps improve only marginally. The main advantage for using crystal-optimized basis sets is to speed up the calculations, due to more contracted exponents, and this becomes more appreciable for larger systems, while the pruned basis sets provide a quick and reliable choice for extensive benchmark purpose.

Table 2.1. Comparison of the performance of pruned and optimized basis sets on structures and band gaps of CuInSe_2 , CuGaSe_2 , and CdS .

basis sets	CuInSe_2				CuGaSe_2				CdS	
	$a/\text{\AA}$	$c/\text{\AA}$	$u(\text{Se})$	E_g/eV	$a/\text{\AA}$	$c/\text{\AA}$	$u(\text{Se})$	E_g/eV	$a/\text{\AA}$	E_g/eV
pruned	5.909	11.899	0.229	1.07	5.729	11.234	0.255	1.58	5.933	2.55
optimized	5.879	11.809	0.226	1.04	5.693	11.192	0.252	1.54	5.930	2.56
<i>Exptl.</i>	5.781	11.642	0.226	1.04 ^a	5.614	11.022	0.259	1.67 ^b	5.811	2.58 ^c

^a Ref. [48]. ^b Ref. [49]. ^c Ref. [50].

For optimizing bulk structures, the reciprocal space was sampled by Γ -centered Monkhorst-Pack scheme[51], with an $8 \times 8 \times 8$ grid. To compute the band structure and DOS a finer $16 \times 16 \times 16$ grid was used on the optimized structure.

2.3 Key ingredients in XC functionals for performance

In order to determine whether any of the common methods for DFT could provide sufficient accuracy, we considered a series of XC functionals for band calculations on the CuInSe₂ and CuGaSe₂ chalcopyrite crystals. This included, at various levels of approximations climbing “Jacob’s ladder” [52]:

- LDA: SVWN[53, 54]
- GGA: BLYP[55, 56], PW91[57], PBE[58]
- meta-GGA: M06-L[59]
- global hybrid GGA: B3PW91[60], B3LYP[61], PBE0[62], BHLYP[63], and screened hybrid GGA: HSE06[64–66]
- global hybrid meta-GGA: M06[67]

Tables 2.2 and 2.3 show that the original hybrid scheme of Becke, B3PW91[60], leads to the lowest errors in the band gaps, with values that are 0.03 eV larger for CuInSe₂ and 0.09 eV smaller for CuGaSe₂. The B3PW91 calculated band structures and DOS are shown in Fig. 2.1 and 2.2, predicting correctly the direct band gap type for both CuInSe₂ and CuGaSe₂. In contrast, LDA(SVWN) leads to a zero band gap for CuInSe₂, while the GGA methods (PW91, PBE, and BLYP) lead to a gap of only 0.01 eV (99 to 100% error!), though the non-hybrid meta-GGA (M06-L) improves slightly with a value of 0.13 eV. Both the global hybrid B3LYP and screened hybrid HSE06 lead to too low a gap by 0.09 and 0.10 eV for CuInSe₂ and 0.27 and 0.20 eV for CuGaSe₂, while PBE0 leads to gaps that are too large (by 0.42 eV for CuInSe₂ and 0.35 eV for CuGaSe₂).

From Tables 2.2 and 2.3 we see that:

- (1) The calculated band gaps increase with the percentage of HF exchange, as pointed out by Yang *et al*[19]. Including exact exchange brings in increased localization of the electronic states, which neutralizes the delocalization error of accompanying conventional XC functionals, and is clearly the key ingredient in obtaining accurate band gaps. The higher tier of “Jacob’s ladder”, meta-GGA, indeed improves over GGA on band gaps, yet slightly, and the derived hybrid meta-GGA, M06, does not perform better than hybrid GGAs, most likely because the percentage of HF exchange is not optimal here.
- (2) B3PW91 is better than the most popular hybrid functional B3LYP for both lattice parameters and band gaps. Kresse *et al.* observed this also on metals[69]. The explanation may be that B3LYP underestimates the correlation energy of the uniform electron gas by about 30%, while B3PW91 was designed to be exact for this limit. This suggests that the periodic valence-electron density in a bulk solid is similar to a uniform electron gas.

Table 2.2. Predicted band gap and lattice parameters for CuInSe₂ chalcopyrite crystal from various levels of XC functionals. Here $\eta = c/2a$ is the tetragonal distortion, and $u(\text{Se})$ is the internal degree of freedom. HF% is the percentage of mixed HF exchange. ΔE_g and $\Delta V\%$ are the absolute and relative errors in band gap and volume, respectively, compared to experiment.

XC	HF%	E_g/eV	$\Delta E_g/\text{eV}$	$a/\text{\AA}$	$c/\text{\AA}$	$\eta = c/2a$	$u(\text{Se})$	$\Delta V\%$
<i>Exptl.</i>	—	1.04 ^a	—	5.781	11.642	1.007	0.226	—
SVWN	0%	0.00	1.04	5.787	11.676	1.009	0.216	0.50%
BLYP	0%	0.01	1.03	6.057	12.196	1.007	0.224	15.00%
PW91	0%	0.01	1.03	5.929	11.953	1.008	0.221	8.00%
PW91 ^b	0%	0.04	1.00	5.836	11.657	0.999	0.221	2.04%
PBE	0%	0.01	1.03	5.935	11.965	1.008	0.222	8.32%
M06-L	0%	0.13	0.91	5.941	12.029	1.012	0.226	9.12%
B3PW91	20%	1.07	0.03	5.911	11.895	1.006	0.229	6.82%
B3LYP	20%	0.95	0.09	5.998	12.046	1.004	0.232	11.38%
PBE0	25%	1.46	0.42	5.892	11.857	1.006	0.230	5.80%
BHLYP	50%	3.37	2.33	5.982	11.945	0.998	0.240	9.86%
HSE06	25%*	0.94	0.10	5.895	11.878	1.007	0.229	6.10%
M06	27%	1.39	0.35	5.887	11.909	1.011	0.226	6.08%

^a Ref. [48]. ^b results from Ref. [68], using plane wave basis sets with USPP.

* screened HF exchange.

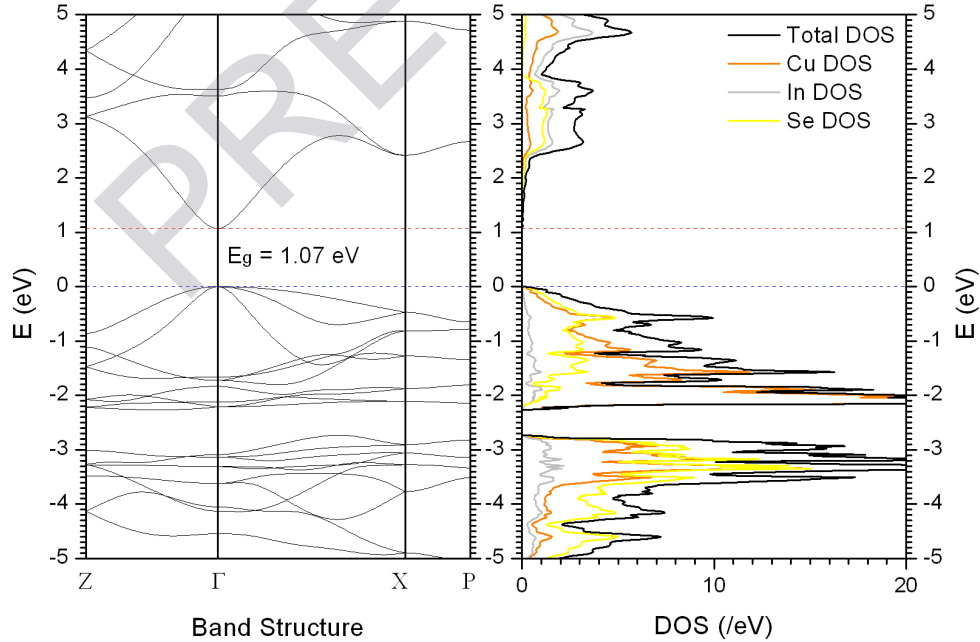


Figure 2.1. The band structure and DOS of CuInSe₂ calculated with B3PW91.